8-8-2023

Enhanced UV Light-Emission of Zinc-Phosphate-Hydrate Hydrothermally-Grown on Cu Metal Substrates for Opto-Electronic Applications

Yuting Spiegelhoff
University of Wisconsin-Milwaukee

Filip Zemajtis
University of Wisconsin-Milwaukee

Elaheh Kheirandish
University of Wisconsin-Milwaukee

Oliver Grauby
University of Aix-Marseille

Daniel Ferry
University of Aix-Marseille

See next page for additional authors

Recommended Citation

Spiegelhoff, Y., Zemajtis, F., Kheirandish, E., Grauby, O., Ferry, D., Pellenq, R. J. -M., Sobolev, K., & Kouklin, N. (2023). Enhanced UV light-emission of zinc-phosphate-hydrate hydrothermally-grown on Cu metal substrates for opto-electronic applications. Advanced Electronic Materials. https://doi.org/10.1002/aelm.202300272

Authors

Yuting Spiegelhoff, Filip Zemajtis, Elaheh Kheirandish, Oliver Grauby, Daniel Ferry, Roland J.-M. Pellenq, Konstantin Sobolev, and Nikolai Kouklin

Enhanced UV Light-Emission of Zinc-Phosphate-Hydrate Hydrothermally-Grown on Cu Metal Substrates for Opto-Electronic Applications

*Yuting Spiegelhoff, Filip Zemajtis, Elaheh Kheirandish, Olivier Grauby, Daniel Ferry, Roland J.-M. Pellenq, Konstantin Sobolev, and Nikolai Kouklin**

In the present study, polycrystalline films of layered zinc phosphate hydrate are produced by a facile, low-temperature single-step hydrothermal fabrication method on top of Cu metal substrates. Despite containing structural water, the as-grown films remain crystalline, chemically stable, and electrically conductive. The photoluminescence spectrum obtained at room-temperature reveals the presence of a spectrally narrow, high-intensity ultraviolet band that consists of two Gaussian peaks at ≈377 and 383 nm and a UV-to-visible peak emission intensity ratio of ≈5.3. The electrical charge-transport properties remain Ohmic for electric fields of up to ≈2 kV m^{-1} and temperature (T) range of ≈223–368 K. The electrical conductivity is further found to vary exponentially with the inverse temperature, and the thermal activation energy, E_a is 285 ± 8 meV. A moderate UV-vis photoconduction effect is registered and assigned to light-assisted electronic transitions that involve near-band edge defect states. This study can potentially open a door to the engineering and deployment of water-based compounds with advanced, semiconducting-like attributes in short-wavelength opto-electronic devices.

1. Introduction

Photoluminescence (PL) enhancement and related development of low-cost, strongly UV-light emitting materials are of central importance to advancing many research fields, such as photonics, optoelectronics, plasmonics, biosensing, and medical diagnostics.[1–6] The PL emission spectra are generally known to vary with chemical composition, crystal structure, defects, physical state parameters such as temperature and pressure, as well as crystal sizes and morphologies.[7,8] Apart from quantum confinement effects, the use of metallic plasmonic nanostructures was actively pursued to achieve strongly-amplified room-temperature (RT) light emission from organic and inorganic materials, including phosphates. Saad et al., for instance, studied Ag nanoparticles (Ag-NPs) induced luminescence enhancement of Eu^{3+}-doped-phosphate glasses. The obtained absorption spectra revealed a surface plasmon resonance band of Ag-NPs[9] and the luminescence enhancement properties of Eu^{3+}-doped-phosphate glass containing Ag-NPs were shown to depend not only on the NPs to Eu^{3+} ions energy transfer but also on NPs surface plasmon resonance. Park et al. [10] also showed that plasmonic nanostructures can control and improve PL yields through localized surface plasmon resonance that results from the interaction between light and metallic

---

Y. Spiegelhoff, E. Kheirandish, N. Kouklin
Departments of Electrical Engineering
University of Wisconsin-Milwaukee
3200 North Cramer St., Milwaukee, WI 53211, USA
E-mail: nkouklin@uwm.edu

F. Zemajtis, K. Sobolev, N. Kouklin
Materials Science and Engineering
University of Wisconsin-Milwaukee
3200 North Cramer St., Milwaukee, WI 53211, USA

The ORCID identification number(s) for the author(s) of this article can be found under https://doi.org/10.1002/aelm.202300272

DOI: 10.1002/aelm.202300272

O. Grauby, D. Ferry
Aix Marseille Univ
CNRS
CINaM
Marseille France

R. J.-M. Pellenq
Epidapo Lab – CNRS / George Washington University
Children's National Medical Center
Children's Research Institute
111 Michigan Ave. NW, Washington, DC 20010, USA

K. Sobolev
Civil Engineering
University of Wisconsin-Milwaukee
3200 North Cramer St., Milwaukee, WI 53211, USA

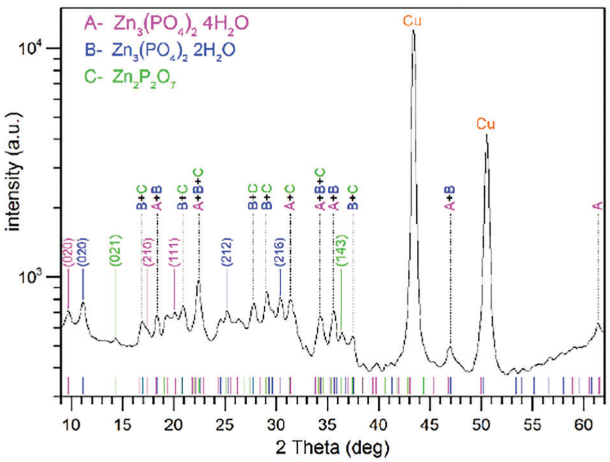

Figure 1. XRD diffractogram of a multilayer film of $Zn_3(PO_4)_2$•$4H_2O$ (phase A, pink), $Zn_3(PO_4)_2$•$2H_2O$ (phase B, blue), and $Zn_2P_2O_7$ (phase C, green) grown on a Cu substrate. The Miller indices of the peaks corresponding to the three identified phases A, B, C are indicated, and the main sum peaks are labeled with the phases from which they originate. A colored collared reference spectrum of each phase is indicated by vertical marks at the bottom.

nanostructures. Rashed et al. [11] studied a hybrid plasmonic system to elucidate the mechanisms governing the luminescent (fluorescent) enhancement process using an antenna effect. Plasmonic nano-disks of various diameters were chosen as receiver and transmitter nano-antennas to effect stronger photoluminescence of adsorbed dye molecules. The enhancement of the spontaneous emission rate was claimed to arise from the superposition of three contributions: (i) metal-enhanced fluorescence, (ii) metal-enhanced excitation, and (iii) plasmon-modulated photoluminescence of the photoexcited nanostructures. Overall, the observed strong emission is attributed to the bi-directional near-field coupling of the fluorescent dye molecules to the localized plasmonic field of nano-antennas.

Among different classes of solids, wide-bandgap compounds remain the most technologically important for the development of compact, short-wavelength, high-power-density light sources and detectors.[12–15] Yet, electronic-grade materials and their heterojunctions, as a rule, are produced under high vacuum in high-cost Molecular Beam Epitaxy (MBE) and Chemical Vapor Deposition (CVD) reactors. The MBE growth remains slow and is done on small-area single-crystal substrates. CVD techniques, on the other hand, demonstrate orders of magnitude larger throughput and are widely used by the semiconductor-device industry to fabricate integrated circuits, solar cells, heterojunctions, and optical coatings.[16–19] As a trade-off, the CVD-synthesized structures tend to be polycrystalline and, therefore, suffer from such detrimental effects as Fermi-level pinning, reduced charge carrier mobility, and an increased role of defect-assisted nonradiative recombinations.

In this study, we have applied a facile single-step hydrothermal fabrication method to produce opto-electronic-grade, layered zinc phosphate hydrate $Zn_3(PO_4)_2$•$4H_2O$ films onto Cu metal substrates. ZnO nanoparticle powders dissolved in phosphoric acid served as the only growth precursors. Despite featuring structural water content, these hydrate films are confirmed to be mechanically and chemically robust. The samples also demonstrate a spectrally narrow room-temperature (RT) UV luminescence band fitted with two Gaussian peaks centered at ≈377 and 383 nm. The charge transport was assessed by performing current-voltage (I–V) measurements, and I–Vs were found to be Ohmic, with the electrical conductivity rising exponentially in the temperature range of ≈223 to 368 K. Below, we also present and discuss the structural, elemental, transport, and light-emission characteristics obtained by carrying out scanning electron microscopy (SEM), Energy dispersive X-ray (EDX), X-ray Diffraction (XRD), Transmission electron microscopy (TEM), PL, and PL-excitation (PLE) measurements.

2. Results and Discussion

2.1. Hydrothermal Fabrication

A ≈99% pure, 25 × 25 mm Cu foil tile supplied by SpeedyMetals was used as a growth substrate. Prior to deposition, the surface of the Cu substrate was sandblasted, ultrasonically cleaned, and air-dried. The precursor-containing solution was prepared by adding ≈99% pure ZnO nanoparticle powder obtained from Sigma–Aldrich to a ≈85% phosphoric acid-water bath with weight ratios of oxide-to-acid and water-to-acid of ~0.4 and 6.0, respectively. The suspension was continuously agitated on a hotplate for ≈15 mins to allow for a full dissolution of the ZnO nanoparticle solid phase.

The multilayer films were grown onto prepared coupons as follows. The first two layers were grown by drop-casting and spin-coating the solution for ≈15 s at ≈1500 RPM speed. The samples were next placed in the oven at ≈105 °C and allowed to dry in the open air for ≈15 mins. A final third layer was spin-coated for ≈15 s using the same speed but followed by ≈1-h sintering at ≈250 °C.

2.2. Characterization Methods

To identify the crystalline phases present and to probe the crystal quality of the multilayer-grown film, XRD measurements were carried out first. For these powders were prepared by scraping off, mechanically reducing by grinding, and finally placing the powders into a glass capillary. The XRD apparatus comprised a high-gloss rotating Cu anode (Rigaku RU-200BH) emitting Cu-K_α radiation ($\lambda = 1.5418$ Å), focusing optics (OSMIC) and planar image-type detector (Mar 345). The scattering intensities were acquired for an angular range of $9° \leq 2\theta \leq 62°$.

The elemental composition was done on scrapped-off pieces of the film that were ultrasonically dispersed in distilled water and drop-cast onto a metal TEM grid. The EDX spectra were collected with a Jeol JEM-2011 TEM, operating at ≈200 keV and equipped with a silicon drift XFlash 5030 detector supplied by Bruker. The electron current density was ≈63 pA cm^{-2}. The electron-selected area diffraction patterns could not be obtained reliably due to a partial loss of the structural integrity of the samples imaged with a high-energy electron beam. To quantify the elemental atomic compositions and for stoichiometric assessments, we used a Bruker AXS TEM software package.

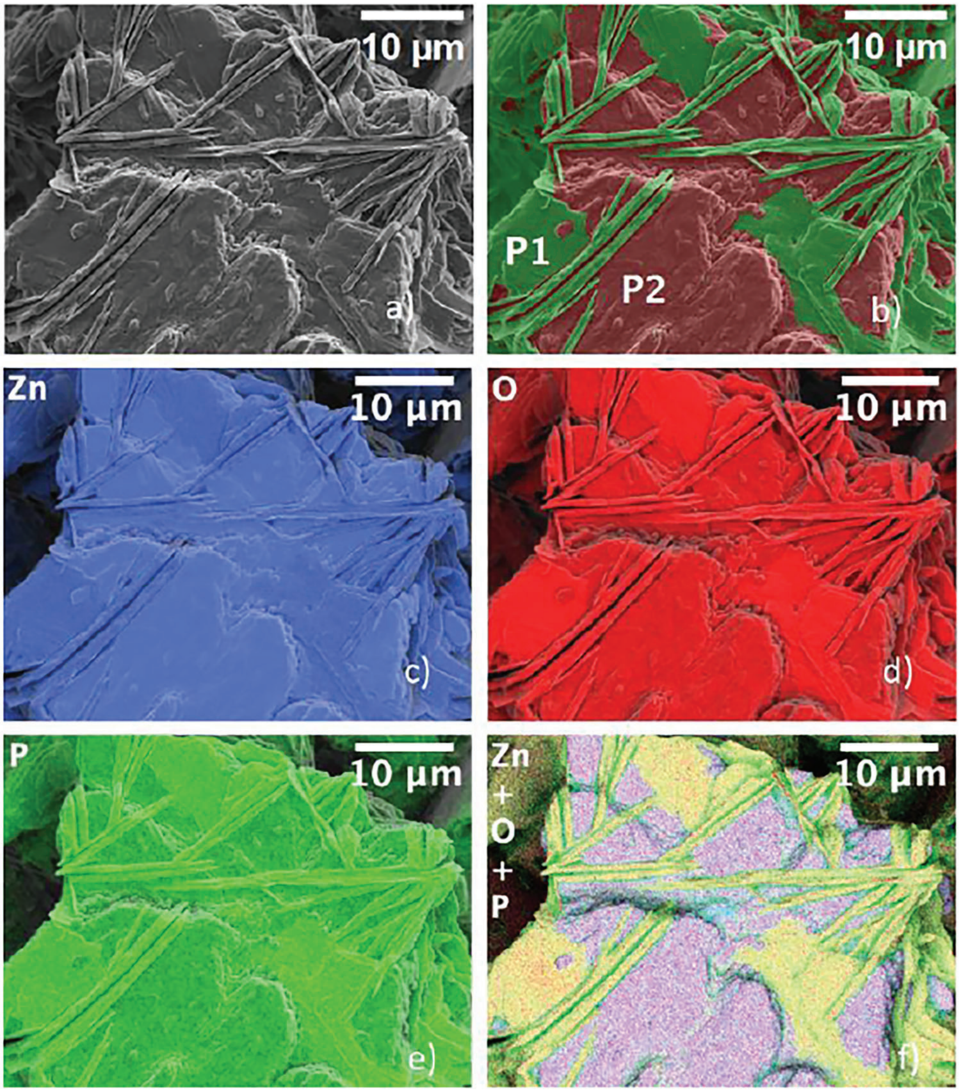

Figure 2. a) SEM image of the grown zinc phosphate film. (b-f) Elemental maps of zinc phosphate film: Zn (blue), O (red), P(green), Zn+O+P and chemical phase mapping of hydrated phase P1 {$Zn_3(PO_4)_2$•$4H_2O$ and/or $Zn_3(PO_4)_2$•$2H_2O$} and pyrophosphate phase P2 ($Zn_2P_2O_7$).

SEM images and 2D elemental chemical maps were collected with the help of a Jeol JSM-7900F microscope operating at a top-view mode and a low accelerating bias of ≈5 keV.

The PL and PLE spectroscopic measurements were done by exciting samples with a spectrally filtered light generated by a Xenon lamp (optical power density of ≈5 mW cm^{-2}). All emission spectra were collected with an Olympus 51X microscope and dispersed by a second double-grating monochromator. A photomultiplier tube operating in a photon counting mode served as a detector. The instrument resolution was limited to ≈1 nm, and the spectral acquisition range was ≈350–680 nm.

Temperature-dependent charge-transport and wavelength-dependent photo-current measurements were carried out with the help of a computer-controlled Keithley-236 source-measure unit. Two-terminal measurements were done by depositing the samples on Cu-Zn electrodes, and cycling the electrical bias from −0.6 to 0.6 V. INSTEC temperature-controlled stage was used for T-dependent *I*–*V* acquisitions.

2.3. Experimental Results and Analysis

A characteristic XRD spectrum is presented in **Figure 1** and consists of an array of individual peaks in confirmation that the films remain polycrystalline. Using X'Pert High Score software, three distinct crystalline phases were detected and assigned to $Zn_3(PO_4)_2$•$4H_2O$ (hopeite), $Zn_3(PO_4)_2$•$2H_2O$ (partially hydrated hopeite), and $Zn_2P_2O_7$ (pyrophosphate). A complete list of the XRD reflections, Miller indices, and relative intensities is given for each phase in the supplementary information. The XRD peaks of ZnO crystalline phases were not detected.

According to a top-view SEM image of the substrate-attached structures, **Figure 2** a, the film comprises aggregates of highly flattened automorphic and prismatic crystals with the lateral dimensions ranging from ≈10 to 100 µm.

The prismatic morphology of the crystals appears very similar to that of the hopeite reported by Milnes.[20] The elemental compositions of $Zn_3(PO_4)_2$•$2H_2O$ and $Zn_3(PO_4)_2$•$4H_2O$ differ

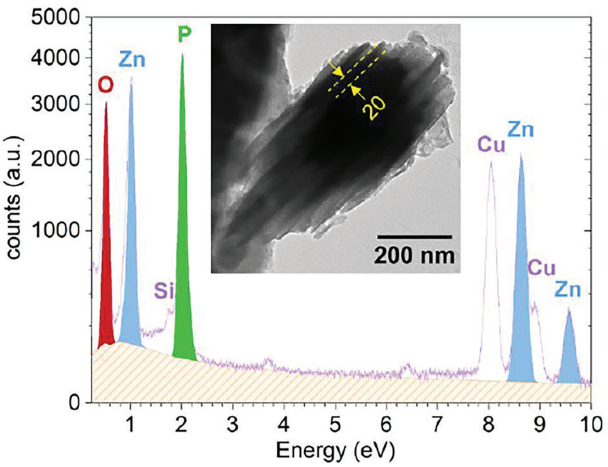

Figure 3. EDX spectrum of prismatic crystals made of Zn, P, and O. Cu signal is to originate from the TEM grid, growth substrate, and the film itself. The inset shows a TEM image of the flattened prismatic crystal of zinc phosphate hydrate, confirming its lamellar structure.

very slightly, and the two hopeite phases remain morphologically similar which make them SEM-indistinguishable. The results of the elemental analysis show that the prismatic crystals are made of elemental Zn, P, and O. In line with SEM, the EDX does not allow us to differentiate between Zn_3 $(PO_4)_2$•$2H_2O$ and Zn_3 $(PO_4)_2$•$4H_2O$ phases. 2D EDX elemental phase maps are shown in Figure 2b–f, which confirms that the automorphic crystals are embedded in the matrix composed of Zn, P, and O. Composition-wise, the prismatic phase is found to be made from ≈55%–60% of [Zn+O] and ≈40%-45% of [2P$_{+}$5O] elemental stochiometric combinations. On the other hand, the chemical composition of the prevailing phase is ≈66% of [Zn+O] and ≈34% of [2P +5O]. According to Panache et al,[21] the chemical composition of hopeite Zn_3 $(PO_4)_2$•$4H_2O$ is ≈63% of [Zn+O] and ≈37% of [2P+5O], while that of $Zn_2P_2O_7$ is ≈67% of [Zn+O] and ≈34% of [2P+5O]. The crystal structure of Zn_3 $(PO_4)_2$•$2H_2O$ is not fully characterized to date.

Based on the SEM-EDX data, we conclude that the prismatic phase consists of crystalline $Zn_3(PO_4)_2$•$4H_2O$ and/or $Zn_3(PO_4)_2$•$2H_2O$, and the remaining phase is likely to be $Zn_2P_2O_7$. These results are generally in agreement with the XRD data presented in Figure 1. A low-resolution TEM image is further provided in **Figure 3**, the inset, and reveals the presence of lamellar crystals, with an interplanar distance of ≈20 nm. Its EDX spectrum is shown in Figure 5, and the chemical composition is found to closely match that of the hopeite but not $Zn_2P_2O_7$. Herschke et al.[22] pointed out that the water molecules that are present in zinc phosphates help promote stable 3D architecture/morphology of the films.

Light emission characteristics of the samples were assessed by carrying out RT PL and PLE spectroscopic measurements. The resultant PL spectrum, **Figure 4** a is dominated by a spectrally sharp, high-intensity UV band and visible-range broad, low-intensity bands with peaks at ≈378 and 495 nm, respectively. Both PL bands exhibit asymmetric right shoulder broadenings, and the spectrum can be fitted with four stand-alone Gaussian peaks at ≈377, 383, 482, and 508 nm, Figure 4a. The RT PLE spectrum was further obtained by collecting PL at ≈495 nm, Figure 4a, the inset. Gaussian spectral decomposition reveals the presence of five individual PLE bands centered at ~303, 326, 357, 372, and 392 nm. The ≈303 and 326 nm PLE bands also appear in the PLE spectrum collected at ≈378 nm. The PL emission at ≈495 nm is primarily excited in the ≈340–400 nm spectral range, and two much weaker ≈303 and 326 nm PLE bands stem from the re-absorption of UV light generated at ≈378 nm. As we use ZnO nanoparticle precursor, it is tempting, yet incorrect, to assign the PL emission to ZnO, as no crystalline ZnO was confirmed for our samples (see prior discussed XRD, EDX, and TEM data). Furthermore, according to Figure 4 a, the inset, the PLE-value of the band gap, E_g is extrapolated to be ≈2.83 eV at ≈300 K. The E_g can approach a low limit of ≈2.8 eV in a highly disordered ZnO, in which, however, the excitonic PL is to be heavily suppressed in favor of a defect-assisted PL.[23] Thus, once again confirming that UV emission cannot originate from ZnO in our case. Likewise, the PL spectrum of $Zn_2P_2O_7$ comprises a very weak, broad PL band centered at ≈450 nm, we equally rule out $Zn_2P_2O_7$ as a source of the observed UV PL.[24]

According to the optical absorption studies done before on zinc-phosphate glasses,[25] the RT band gap, E_g is reportedly ≈3.39–3.68 eV. PLE findings point to the existence of two separate excitation-emission pathways for UV and visible-range PL, Figure 4b the left and right schematics. This can be explained by the presence of two indistinguishable crystalline sub-phases, as identified earlier. The PLE-obtained E_g of ≈2.83 is attributed to a weaker, visible-range emitting more disordered sub-phase of the zinc phosphate hydrate. The formation of the band-edge defect states is a known reason behind a reduced band gap of polycrystalline materials.

It needs to be mentioned that a strong UV PL was only registered in the films grown on Cu but not on stainless-steel substrates, with the latter promoting the formation of structurally-different hopeite films (XRD data, not shown). The enhanced emission can be due to an interplay of several factors: (i) a larger rate of excitation, (II) a larger rate of emission, or (III) an increased percentage of emitting versus nonemitting phase. Exposure of Cu substrates to acidic baths can also lead to unintentional assimilation of EDX-undetectable Cu traces within the films; the former could act as PL amplification centers, as discussed above. Likewise, local field amplification effects invoked by a multilayer structure, dielectric interfaces, and highly polarizable intermediate such as water can also strongly influence spontaneous emission rates. [26–29] However, additional work will be required to fully elucidate the contribution of the above-mentioned mechanisms to the light emission of our samples.

We finally discuss the results of temperature-dependent charge-transport and wavelength-dependent photo-current measurements as they are to provide further insights into the electronic properties and charge carrier behavior of the samples. According to **Figure 5**, the *I–V*s remain Ohmic/nonrectifying in the temperature range of ≈223–358 K and for electric field strengths of up to ≈2 kV m^{-1}. Thus, current-limiting Schottky barriers and band offsets known to form at the contacts and interfaces made by different crystalline phases must be ruled out as playing any significant role. Notably, no current hysteresis

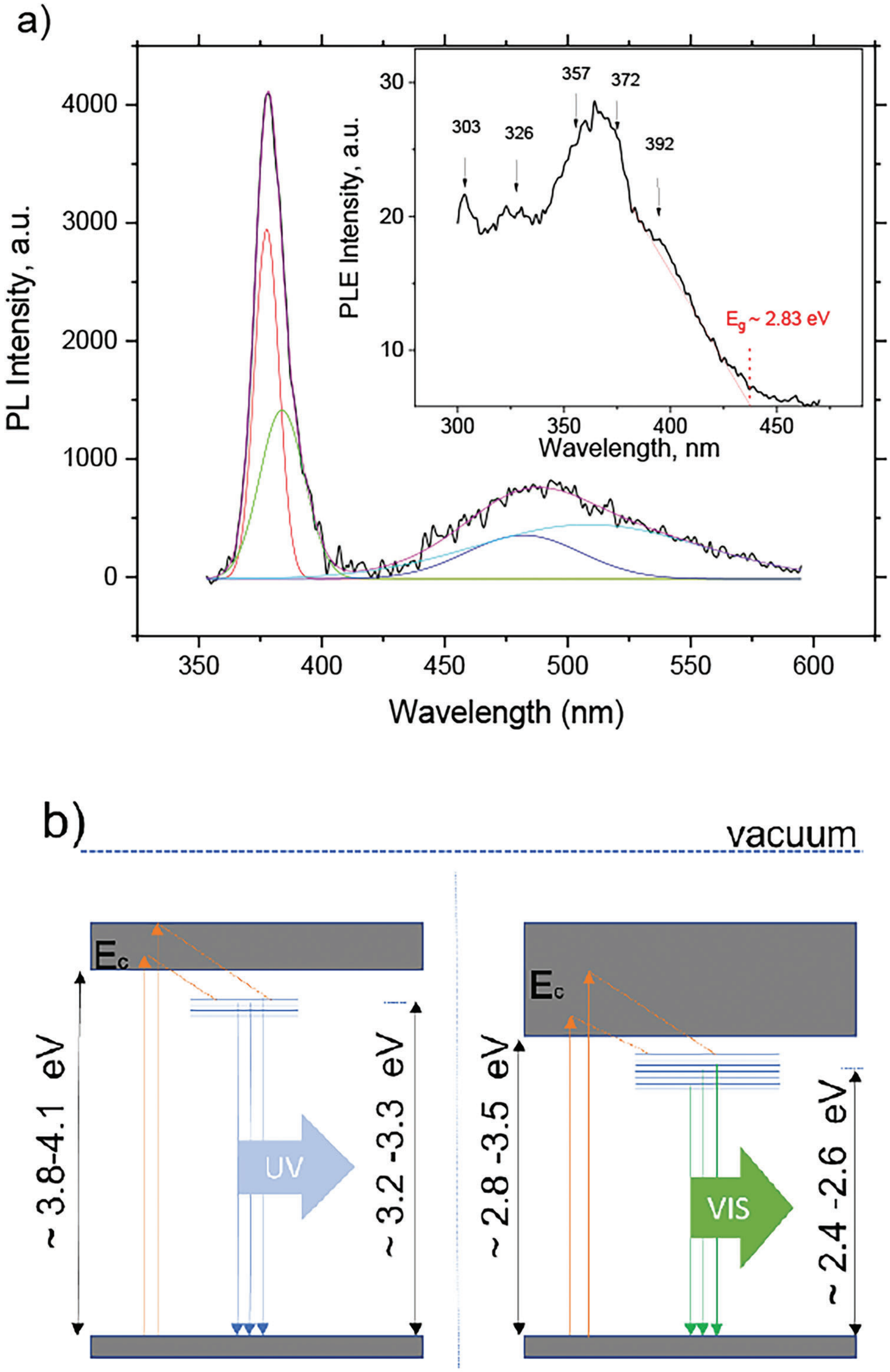

Figure 4. a) RT PL spectrum (black) excited at ≈320 nm and Gaussian fitted with 4 peaks at ≈377, 383, 482, and 508m; the inset shows PLE spectrum (495 nm) with five peaks obtained by Gaussian fitting (not shown): 303, 326, 357, 372, and 392 nm. The band edge is extrapolated to ≈2.83 eV. b) Schematics of the dominant electronic excitation-emission (red-blue and red-green) transitions underlying the UV and visible RT PL, as discussed in the text, after RT-PL and PLE data.

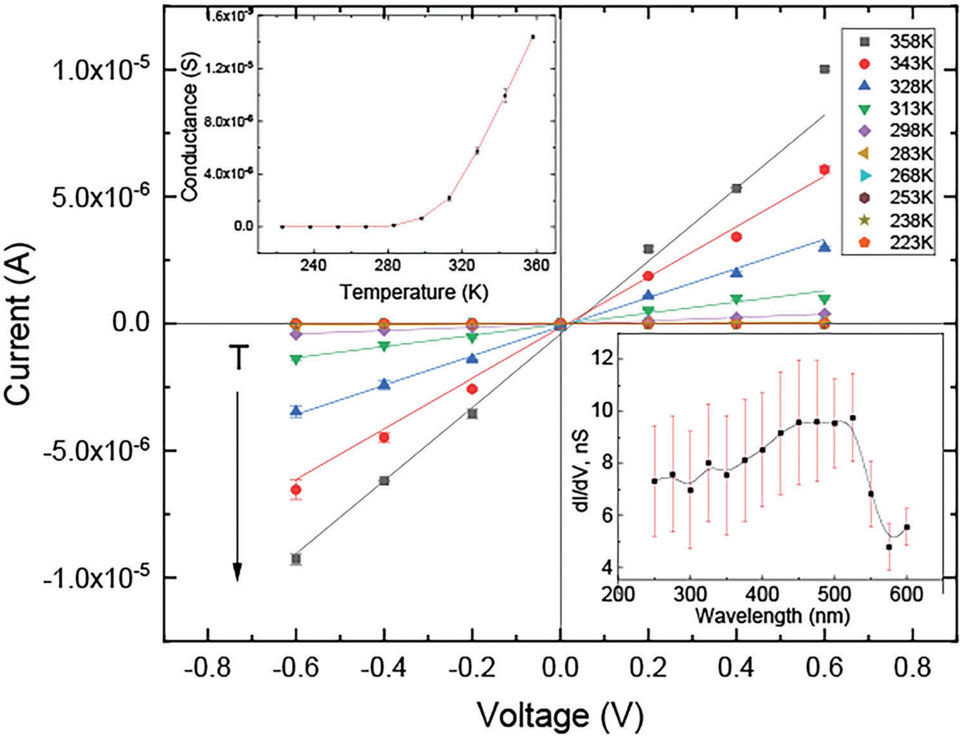

Figure 5. Current-voltage characteristics of the films obtained at varying T of ≈223–358 K. The inset shows conductance versus T plot, and the data were fitted with Arrhenius expression yielding E_a of 285±8 meV. The plot of intensity-normalized differential conductance versus light wavelength obtained at ≈0 V is shown in the lower left inset.

(charge polarization effects) due to the transient nature of the electrical bias is observed.

A zero bias differential conductance, G, was additionally obtained and is found to increase nonlinearly with T, Figure 5, the left inset. As ln(G) versus 1/T plot can be well fitted with a line, the conductivity dependence of T is confirmed to be of the Arrhenius-type. The data fitting with the Arrhenius expression yields an activation energy, E_a, of 285 ± 8 meV. This points to the existence of near band-edge defect states (band-to-defect state electronic transitions) that are to act as a primary source of the free charge carriers in the temperature range of ≈223–358 K. The plot of the intensity-normalized G as a function of light wavelength was obtained in the spectral range of ≈240–600 nm, Figure 5, the right low inset. While rising in the ≈240–520 nm range, G undergoes a strong decline starting at ≈520 nm. The onset coincides with the defect excitation energy of ≈2.4 eV, Figure 4b indicating the defect states that induce visible-range emission are also behind the photo-conduction effect. While ionic conductivity cannot be entirely ruled out, the results point to the charge transport, i.e., electrical drift primarily taking on the electronic rather than ionic origin; the latter is more typical of the phosphate glasses containing alkali impurities.[30] The observed positive photoconduction effect can be understood as follows. Under illumination, the empty defect states are to be repopulated forcing the quasi-Fermi level to upshift. In turn, the free charge carrier density increases in the conduction band, and the electrical conductivity rises. Under this indirect excitation scenario, the photoconduction effect is expected to be relatively moderate, in line with the experimental findings.

3. Conclusion

A one-step, low-temperature hydrothermal growth technique was used to produce crystalline films in $Zn_3(PO_4)_2{\bullet}4H_2O$/$Zn_3(PO_4)_2{\bullet}2H_2O$ on top of Cu metal substrates. While the films incorporate water as a part of their structure, they remain mechanically robust and chemically stable. The films exhibit Ohmic *I*–*V*s and electronic semiconductor-like charge transport characteristics. The RT photoluminescence remains unexpectedly strong, and the spectrum is dominated by two UV-Gaussian peaks at ≈377 and 383 nm. The electrical conductivity is found to remain thermally activated for T >283 K with the activation energy of ≈285 meV. A moderate RT UV-vis photoconduction effect is observed and attributed to the light-assited electronic transitions involving defect states. The study opens a door to a facile bottom-up synthesis of hydrated- solids for potential application in low-cost solid-state short-wavelength light sources and light sensors.

Supporting Information

Supporting Information is available from the Wiley Online Library or from the author.

Acknowledgements

The work at UWM was supported by NSF Rapid Award No. 2028535, NSF PIRE, and UWM RGI grants (K.S. and N.K.). The authors would like to thank R. A. Huerta and R. T. Heintzkill for their assistance with sample characterization.

Conflict of Interest

The authors declare no conflict of interest.

Data Availability Statement

The data that support the findings of this study are available from the corresponding author upon reasonable request.

Keywords

current, emissions, hydrothermal, light, zinc phosphate hydrate

Received: April 26, 2023
Revised: June 26, 2023
Published online:

[1] P. Michler, A. Kiraz, C. Becher, W. V. Schoenfeld, P. M. Petroff, L. Zhang, E. Hu, A. Imamoglu, *Science* **2000**, *290*, 2282.
[2] X. Gao, Y. Cui, R. M. Levenson, L. W. K. Chung, S. Nie, *Nat. Biotechnol.* **2004**, *22*, 969.
[3] M. Tebyetekerwa, J. Zhang, Z. Xu, T. N. Truong, Z. Yin, Y. Lu, S. Ramakrishna, D. Macdonald, H. T. Nguyen, *ACS Nano* **2020**, *14*, 14604.
[4] I. L. Medintz, H. T. Uyeda, E. R. Goldman, H. Mattoussi, *Nat. Mater.* **2005**, *4*, 435.
[5] A. Vardi, N. Akopian, G. Bahir, *Appl. Phys. Lett.* **2006**, *88*, 143101.
[6] R. Bratschitsch, A. Leitenstorfer, *Nat. Mater.* **2006**, *5*, 855.
[7] D. W. G. Ballentyne, *Prog. Solid States Chem* **1964**, *1*, 209.
[8] S. P. Wang, S. L. Zhong, H. L. Xu, *J. Phys.: Conf. Ser.* **2009**, *188*, 012034.
[9] M. Saad, W. Stambouli, S. A. Mohamed, H. Elhouichet, *J. Alloys Compd.* **2017**, *705*, 550.
[10] J.-E. Park, J. Kim, J.-M. Nam, *Chem. Sci.* **2017**, *8*, 4696.
[11] A. R. Rashed, M. Habib, N. Das, E. Ozbay, H. Caglayan, *New J Phys* **2020**, *22*, 093033.
[12] S. Nakamura, T. Mukai, M. Senoh, *Appl. Phys. Lett.* **1994**, *64*,1687.
[13] S. Nakamura, M. Senoh, S. Nagahama, N. Iwasa, T. Yamada, T. Matsushita, H. Kiyoku, Y. Sugimoto, *Jpn. J. Appl. Phys.* **1996**, *35*, L74.
[14] I. Akasaki, H. Amano, M. Kito, K. Hiramatsu, *J. Lumin.* **1991**, *48*, 666.
[15] H. Morkoc, S. Strite, G. B. Gao, M. E. Lin, B. Sverdlov, M. Burns, *J. Appl. Phys.* **1994**, *76*, 1363.
[16] Y. Zhao, Z. Li, S. He, X. Liao, S. Sheng, L. Deng, Z. Ma, *Sol. Energy Mater. Sol. Cells* **1997**, *48*, 321.
[17] R. J. Molnar, W. Gotz, L. T. Romano, N. M. Johnson, *J. Cryst. Growth* **1997**, *178*, 147.
[18] B. C. Chung, M. Gershenzon, *J. Appl. Phys.* **1992**, *72*, 651.
[19] C. Niikura, A. Masuda, H. Matsumura, *J. Appl. Phys.* **1999**, *86*, 985.
[20] A. R. Milnes, R. J. Hill, *Neues Jahrbuch fur Mineralogie- Abhandlungen* **1977**, *1*, 25.
[21] C. Palache, H. Berman, C. Frondel, in *Dana's System of Mineralogy* (7th ed.), *2*, John Wiley & Sons, Inc., New Jersey, USA **1951**, 734.
[22] L. Herschke, V. Enkelmann, I. Lieberwirth, G. Wegner, *Chem. - Eur. J.* **2004**, *10*, 2795.
[23] A. Gupta, M. Omari, N. Kouklin, *J. Appl. Phys.* **2008**, *103*, 124312.
[24] S. K. Gupta, N. Pathak, M. Sahu, V. Natarajan, *Adv. Powder Technol.* **2014**, *25*, 1388.
[25] M. A. Ghauri, W. H. Bokhari, F. M. Nazar, *Int. J. Electron.* **1981**, *51*, 201.
[26] K. H. Drexhage, *J. Lumin.* **1970**, *1–2*, 693.
[27] E. Yablonovitch, T. J. Gmitter, R. Bhat, *Phys. Rev. Lett.* **1988**, *61*, 2546.
[28] E. Yablonovitch, *Phys. Rev. Lett.* **1987**, *58*, 2059.
[29] R. Syed, D. L. Gavin, C. T. Moynihan, *J. Am. Ceram. Soc.* **1982**, *65*, c129.
[30] I. Oliva, A. Masuno, H. Inoue, H. Tawarayama, H. Kazoe, *Solid State Ionics* **2012**, *206*, 45.